ARTICLE   **Open Access**

Semiconductor-free nanoplasmonic photoelectrochemistry of H$_2$O$_2$ over Ag nanowires

Ying-Chu Chen [1], Ying-Zhen Chen[2] and Yu-Kuei Hsu[2]

Abstract

Nanoplasmonics is currently experiencing an ongoing renaissance as a result of the booming research interest in LSPR-mediated but semiconductor-free photocatalysis and photoelectrochemistry directly over nanometals with excellent catalytic activity and conductive properties. To shed light on the underlying mechanism, the present study puts forward H$_2$O$_2$ as the probe molecule, with which the electroreduction at the phase boundary with photoexcited Ag nanowires (NWs) was systemically investigated. In particular, the reaction rate depends not only linearly on the illumination intensity but also on the resonant wavelength of the characteristic LSPR of the Ag NWs, evidently illustrating that the photoelectrochemical H$_2$O$_2$ reduction is mediated by the LSPR-induced energetic electrons of the Ag NWs. In addition to the mechanistic insights, the present study further highlights the great promise of such semiconductor-free LSPR-mediated photoelectrochemistry of H$_2$O$_2$ over Ag NWs in the analytical biochemistry field via proof-of-concept solar photoelectrochemical detection of ultradiluted H$_2$O$_2$ in PBS. The Ag NWs deposited on a carbon cloth substrate as the working electrode exhibit excellent sensitivity amounting to 118 µA cm^{-2} mM^{-1} under solar illumination, well outperforming that of the electrochemical counterpart measured in the dark by 50%.

Introduction

For decades, nanoplasmonics, particularly the localized surface plasmon resonance (LSPR) of primarily coinage metals (e.g., Au, Ag, and Cu) designed in a variety of nanoarchitectures, has been an important subject in the areas of broadband sunlight-driven chemical conversion for fuel generation and environmental remediation via semiconductor photocatalysis and photoelectrochemistry[1–4]. Conventionally, research attention has focused mostly on the near-field mechanisms at the plasmonic metal/semiconductor photocatalyst solid–solid interface, including (i) the LSPR-triggered strong electric field reinforcing electron–hole pair photogeneration in the semiconductor and (ii) the LSPR-mediated injection of energetic carriers photoexcited first in the plasmonic metal with subsequent transfer to the semiconductor through the in-between

Schottky junction[1–4]. By contrast, such LSPR-induced charge kinetics at alternative plasmonic metal/chemical reactant solid–liquid or solid–gas phase boundaries were relatively overlooked until very recently[4–11]. Several schemes, including the LSPR-mediated excitation, injection, and transfer of the charge carriers to the unoccupied orbitals of the adsorbed molecules through the radiative and nonradiative Landau and chemical interface damping processes, respectively, have been proposed[4–6]. This, along with the seminal works done by pioneers including Linic[5,7], Christopher[6], Nordlander[8–10], Halas[8–10], and so forth[11] successfully demonstrating the photo(electro)chemistry directly on the surface of plasmonic metals, has stimulated tremendous research interest in gaining further insights into such plasmonic-carrier-driven reaction kinetics[4–6]. Motivated by such a pressing need, in the present study, a systematic investigation into the interfacial charge transfer mechanism between photoexcited plasmonic silver (Ag) in a wire-like nanostructure and a hydrogen peroxide (H$_2$O$_2$) probe molecule was carried out. Herein, the Ag nanowire (NW) especially stands out, attributed to its

Correspondence: Yu-Kuei Hsu (ykhsu@gms.ndhu.edu.tw)
[1]China-UK Low Carbon College, Shanghai Jiao Tong University, No. 3, Yinlian Road, Lingang, Shanghai 201306, People's Republic of China
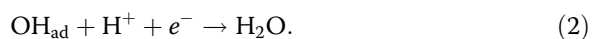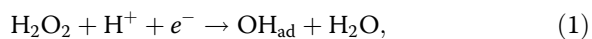[2]Department of Opto-Electronic Engineering, National Dong Hwa University, No. 1, Sec. 2, Da Hsueh Road, Shoufeng, Hualien 97401, Taiwan

outstanding absorption efficiency with respect to those of Au and Cu in harvesting broadband sunlight to photo-excite the characteristic LSPR[1,3–5,7,12]. Moreover, the superior catalytic activity and conductive nature of Ag not only facilitate LSPR-mediated carrier transfer at the interface with H_2O_2 but also, more importantly, allow such delivery to be readily tracked via an electrochemical method[13–15]. To this end, in the present study, Ag NWs were deposited on a conductive carbon cloth (CC) substrate to formulate a Ag/CC working electrode that was further coupled with additional counter and reference electrodes to build a three-electrode cell to register the LSPR-mediated charge transport at the Ag/H_2O_2 solid–liquid junction. Additionally, in the present model system, H_2O_2 was employed as the probe molecule in light of its excellent redox reactivity, as manifested by its ubiquitous utilization in a variety of chemical, biological, and agricultural industries and energy-related applications, e.g., fuel cells[16–19]. For instance, H_2O_2 has been proposed as a promising chlorine-free alternative and employed intensively as oxidative bleaching and disinfection agents in the pulp industry and aquaculture for paper and food production, respectively[16,17]. Such high activity, however, has rendered H_2O_2 the reactive oxygen species (ROS) reported to most likely mediate cellular pathology and numerous neurodegenerative disorders, e.g., Parkinson's disease[16]. In this regard, it is highly desirable to control H_2O_2 at trace levels by transforming redundant H_2O_2 into environmentally and ecologically friendly water (H_2O) for not only biological but also energy-related applications. This chemical reaction is of particular significance to fuel cells, provided that it is well acknowledged as the rate-determining step for the most challenging oxygen reduction reaction that preferentially proceeds via a cascade two-electron reduction mechanism with H_2O_2 as the intermediate over most noble-metal-based cathodes of fuel cells[18,19]. This is well attested in our previous studies by the large overpotential to activate the electroreduction of H_2O_2 over the noble metal Ag[13,14]. Moreover, it is further reinforced by additional reports in the literature, which have demonstrated similar results and, more importantly, further concluded that the reaction rate of H_2O_2 electroreduction is mostly limited by the dissociative adsorption of H_2O_2 to form the OH_{ad} moiety on the Ag surface (Eq. 1)[20,21].

$$H_2O_2 + H^+ + e^- \rightarrow OH_{ad} + H_2O, \tag{1}$$
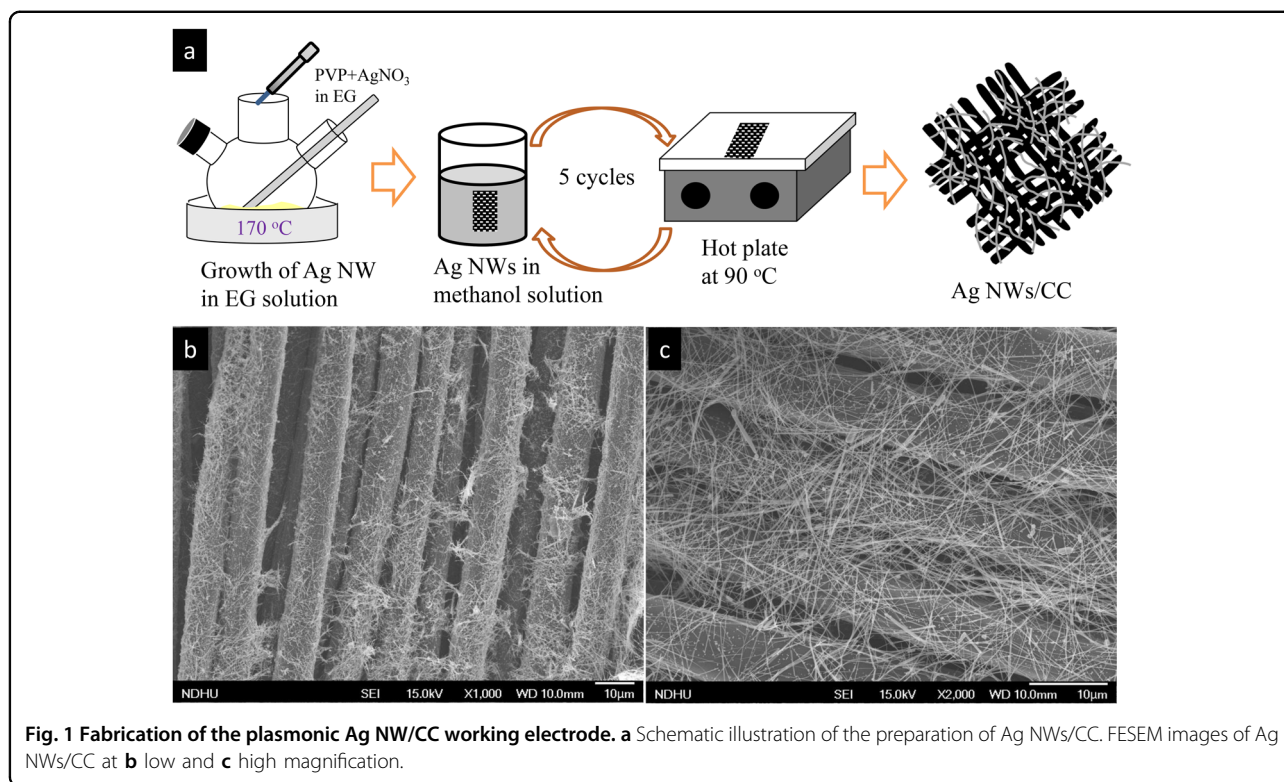
$$OH_{ad} + H^+ + e^- \rightarrow H_2O. \tag{2}$$

In this context, in the present research, H_2O_2 electroreduction was employed as the probe chemical reaction to shed light on the LSPR-mediated charge kinetics at the Ag/H_2O_2 interface, in which the reaction rate was first tracked by means of cyclic voltammetry (CV) and chronoamperometry. After the NW Ag/CC plasmonic electrode was illuminated by broadband sunlight, a cathodic photocurrent was readily observed in these measurements, providing a clear indication of the expedited reaction rate of H_2O_2 electroreduction. More importantly, this, along with the linear dependence of the photocurrent response on the light intensity and the excellent agreement between the additionally collected photocurrent action spectrum and the optical absorption spectrum, enable clear assignment of the LSPR-mediated energetic electron injection from Ag to H_2O_2 to such acceleration[4–11]. Last but not least, proof-of-concept LSPR-mediated detection of H_2O_2 by a solar-illuminated Ag NW/CC electrode, in which the sensitivity exceeded that of the electrochemical counterpart by 50%, well illustrated the great promise of this semiconductor-free nanoplasmonic photoelectrochemistry.

Materials and methods

All chemicals and reagents were of analytical grade and directly utilized without further purification. The fabrication of the plasmonic Ag NW/CC photoelectrode is schematically depicted in Fig. 1a, which commenced with the preparation of NW Ag colloids[14]. To this end, 50 mL ethylene glycol was first refluxed in a three-necked flask at 170 °C for 1 h, to which 0.5 mM $CuCl_2$ in 6 mL ethylene glycol was subsequently added rapidly. This reaction reservoir was briefly reacted for 5 min, to which addition of 0.05 M silver nitrate ($AgNO_3$) and 0.15 M poly(*N*-vinyl-2-pyrrolidone) (PVP with a molar mass of 58,000 g mol^{-1}) in 44 mL ethylene glycol immediately followed. This reaction reservoir was further reacted for 2 h, and the color gradually transitioned from yellow to black. Afterward, the NW Ag precipitates were first cleaned several times with deionized water to remove the excess PVP and additional residues, subsequently collected via glass filtration and eventually dispersed in methanol. The CC substrate was then immersed in this suspension for 5 min for the deposition of Ag NWs, subsequently placed on a hot plate and heated at 90 °C for 10 min. In this way, the methanol was evaporated, and the Ag NWs were in turn immobilized on the CC substrate. The deposition and post-thermal treatment was denoted herein as one cycle, and five cycles were employed to prepare the plasmonic Ag NW/CC photoelectrode.

The morphology and crystalline structure of Ag NWs/CC were investigated via scanning electron microscopy (SEM, JEM-4000EX operated at 15 kV), transmission electron microscopy (TEM, FEI Tecnai G2 Spirit operated at 120 kV), and X-ray diffractometry (XRD, Bruker D8 Advance diffractometer using Cu K_α radiation with a wavelength of 0.15406 nm). The chemical state of the constituent elements of Ag NWs/CC was studied through

Fig. 1 Fabrication of the plasmonic Ag NW/CC working electrode. a Schematic illustration of the preparation of Ag NWs/CC. FESEM images of Ag NWs/CC at **b** low and **c** high magnification.
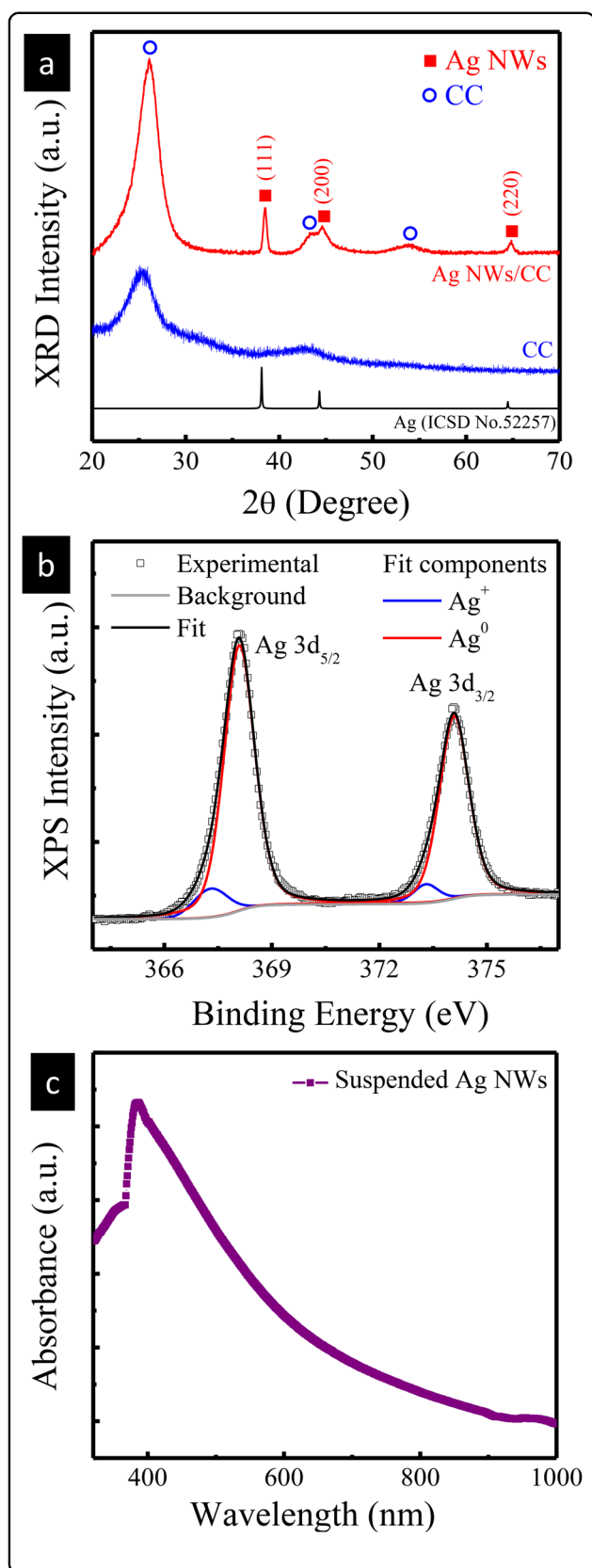
X-ray photoelectron spectroscopy (Perkin-Elmer model PHI 1600). The (photo)electrochemical characteristics of Ag NWs/CC were measured in a phosphate buffer solution (PBS, 0.1 M, pH 7.4) using a potentiostat/galvanostat (CHI 6273D). A conventional three-electrode cell configuration was implemented, consisting of Ag NWs/CC as the working electrode, a square platinum sheet as the auxiliary electrode, and an Ag/AgCl reference electrode in 3 M KCl solution (Supplementary Fig. S1). The potentials reported in this article were with respect to Ag/AgCl (3 M KCl, 0.207 V vs. SHE). A 150 W Xe lamp (Optical Building Blocks Corporation, USA) coupled with an AM 1.5 filter (Newport Corp., USA) was used as the simulated sunlight source with a calibrated light intensity of 100 mW cm^{-2}. In addition, six monochromatic laser diodes (Thorlabs, Inc., USA) with individual wavelengths of 405, 450, 532, 658, 808, and 980 nm were alternatively employed as the light sources in the determination of the wavelength-dependent incident photon-to-current efficiency (IPCE) of the plasmonic Ag NW/CC photoelectrode. The intensity loss of the incident light upon passing through the quartz window and the electrolyte was not considered herein.

Results and discussion

Structural and compositional characterization

SEM was first carried out to investigate the morphology of Ag NWs/CC, which consisted of numerous Ag NWs distributed over each carbon fiber of the CC substrate, for

which the average diameter was ~120 nm and the length was ~10 μm (Fig. 1b, c). XRD was further performed to study the crystalline structure of Ag NWs/CC (Fig. 2a). In addition to the X-ray diffractions (marked with blue hollow spheres) of the underlying CC substrate, only the (111), (200), and (220) X-ray reflections (labeled with red solid squares) of face-centered cubic (fcc) metallic Ag (ICSD no 52257) are seen in the collected XRD pattern. This is in line with the XP spectrum collected at the binding energy of the Ag 3d core level, wherein the measured features were first deconvoluted to give the two most intense emission lines at ~368 and ~374 eV, which are assigned to Ag^0 3$d_{5/2}$ and 3$d_{3/2}$, respectively (Fig. 2b)[14]. Alongside are two tails at ~367 and ~373 eV, which are indexed to Ag$^+$ 3$d_{5/2}$ and 3$d_{3/2}$, respectively, arising presumably from the residues of the Ag$^+$-containing precursor and/or the amorphous Ag$^+$ oxides formed most likely via surface oxidation of the Ag NWs upon exposure to air during the post-thermal treatment (Supplementary Fig. S2). Nevertheless, the weak intensity and the absence of the characteristic X-ray diffractions in the measured XRD pattern suggest a very minor presence of these impurities in Ag NWs/CC (Fig. 2a, b and Supplementary Fig. S2). UV–visible (UV–vis) spectroscopy was additionally conducted to explore the optical property of the Ag NWs suspended in methanol, for which the photoabsorption peaked at ~400 nm, in excellent agreement with the characteristic resonant
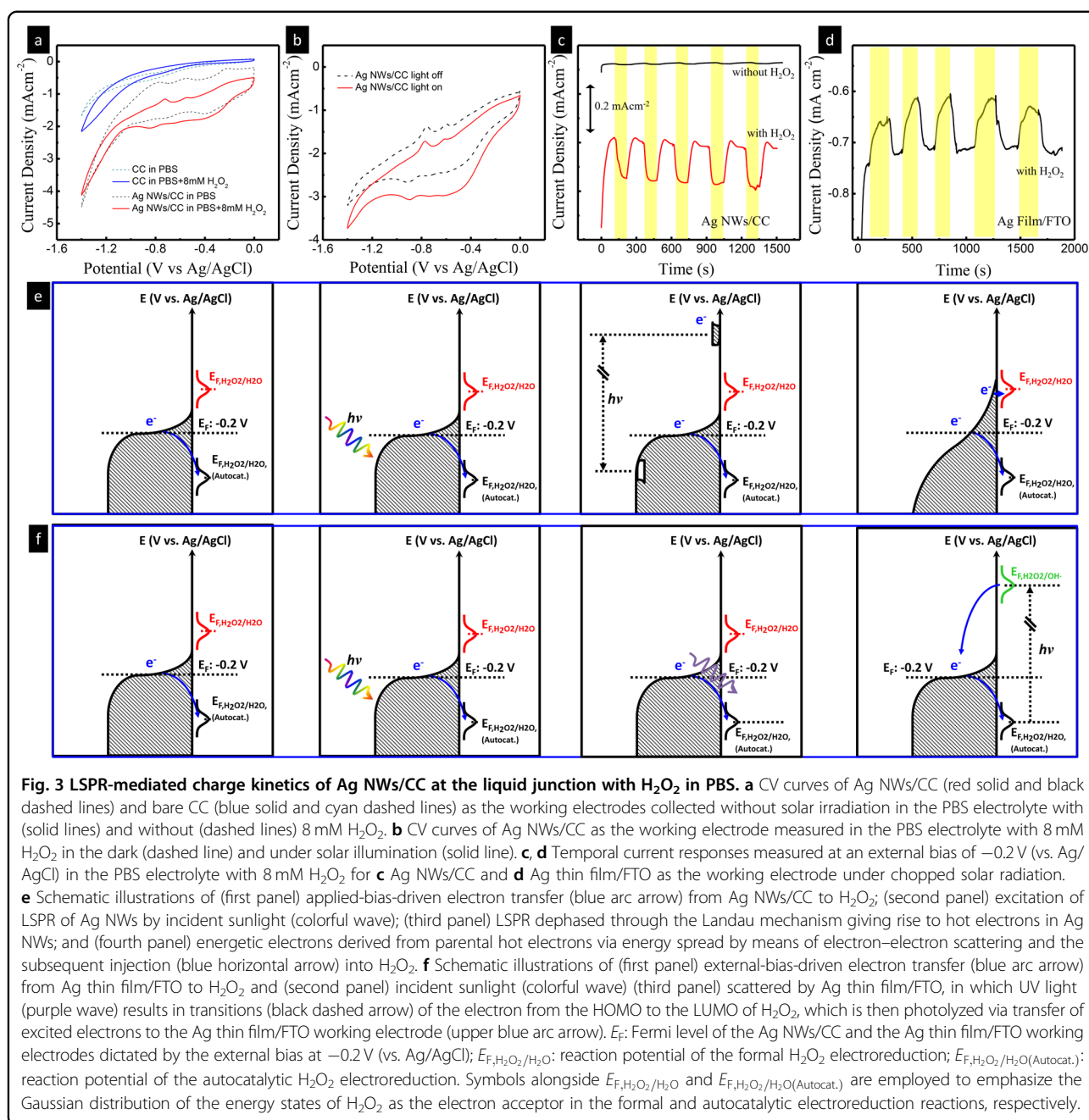
Fig. 2 Material characterization of the plasmonic Ag NW/CC working electrode. a X-ray diffraction patterns of CC (blue solid line) and Ag NWs/CC (red solid line). The features pertaining to CC and Ag NWs are marked with blue hollow spheres and red solid squares. Alongside is the reference pattern (black solid line) of standard Ag (ICSD no. 52257). **b** Ag 3d core-level XP spectrum (black hollow square) of Ag NWs/CC along with the Shirley background (gray solid line) and deconvoluted contributions from monovalent (Ag^+, blue solid line) and metallic (Ag^0, red solid line) silver. **c** Absorption spectrum of the Ag NWs suspended in methanol.

wavelength of the transverse-mode LSPR (T-LSPR) of Ag NWs reported in the literature (Fig. 2c)[1,5,13,22]. In addition to T-LSPR, the LSPR along the longitudinal direction (L-LSPR) of Ag NWs with a high aspect ratio has been reported to account for the broadband absorption of visible and near-infrared light.

LSPR-mediated charge kinetics of Ag NWs/CC at the liquid junction with H_2O_2

CV was first implemented to study the charge kinetics at the solid–liquid junction between Ag NWs/CC as the working electrode and 8 mM H_2O_2 in PBS as the electrolyte. The measurement was performed within a potential range of −1.4 to 0 V (vs. Ag/AgCl) at a scan rate of 50 mV s^{-1}. The cyclic voltammograms of Ag NWs/CC were collected not only in the presence (red solid line) but also in the absence (black dashed line) of 8 mM H_2O_2 in PBS (Fig. 3a). Also shown are the CV curves (blue solid and cyan dashed lines) of bare CC measured under the equivalent conditions for comparison. At first glance, the area under the CV curves of Ag NWs/CC far exceeds that of CC at potentials less than ~−1 V (vs. Ag/AgCl), implying augmented electrosorption due presumably to the appreciable specific surface area additionally offered by the Ag NWs after deposition on the CC substrate (Fig. 1a, b)[20,21]. However, this discrepancy is masked by the current leap at potentials beyond ~−1 V (vs. Ag/AgCl), which corresponds to the onset potential of the hydrogen evolution reaction via water electrolysis (Fig. 3a). Moreover, an additional offset along the cathodic current direction of the entire cyclic voltammograms of Ag NWs/CC with respect to those of bare CC was further perceived from this comparative study. This implies that the measured current flow for Ag NWs/CC comprises not only the capacitive contribution from the foregoing electrosorption but also an extra faradaic contribution probably from electroreduction of the Ag^+-containing residues and/or surface oxides (Fig. 2b and Supplementary Fig. S2), for which the standard reaction potential has been reported to be ~0.8 V (corresponding to ~0.15 V vs. Ag/AgCl in the present model system)[15,20]. Notably, such a

Fig. 3 LSPR-mediated charge kinetics of Ag NWs/CC at the liquid junction with H_2O_2 in PBS. a CV curves of Ag NWs/CC (red solid and black dashed lines) and bare CC (blue solid and cyan dashed lines) as the working electrodes collected without solar irradiation in the PBS electrolyte with (solid lines) and without (dashed lines) 8 mM H_2O_2. **b** CV curves of Ag NWs/CC as the working electrode measured in the PBS electrolyte with 8 mM H_2O_2 in the dark (dashed line) and under solar illumination (solid line). **c, d** Temporal current responses measured at an external bias of -0.2 V (vs. Ag/AgCl) in the PBS electrolyte with 8 mM H_2O_2 for **c** Ag NWs/CC and **d** Ag thin film/FTO as the working electrode under chopped solar radiation. **e** Schematic illustrations of (first panel) applied-bias-driven electron transfer (blue arc arrow) from Ag NWs/CC to H_2O_2; (second panel) excitation of LSPR of Ag NWs by incident sunlight (colorful wave); (third panel) LSPR dephased through the Landau mechanism giving rise to hot electrons in Ag NWs; and (fourth panel) energetic electrons derived from parental hot electrons via energy spread by means of electron–electron scattering and the subsequent injection (blue horizontal arrow) into H_2O_2. **f** Schematic illustrations of (first panel) external-bias-driven electron transfer (blue arc arrow) from Ag thin film/FTO to H_2O_2 and (second panel) incident sunlight (colorful wave) (third panel) scattered by Ag thin film/FTO, in which UV light (purple wave) results in transitions (black dashed arrow) of the electron from the HOMO to the LUMO of H_2O_2, which is then photolyzed via transfer of excited electrons to the Ag thin film/FTO working electrode (upper blue arc arrow). E_F: Fermi level of the Ag NWs/CC and the Ag thin film/FTO working electrodes dictated by the external bias at -0.2 V (vs. Ag/AgCl); $E_{F,H_2O_2/H_2O}$: reaction potential of the formal H_2O_2 electroreduction; $E_{F,H_2O_2/H_2O(Autocat.)}$: reaction potential of the autocatalytic H_2O_2 electroreduction. Symbols alongside $E_{F,H_2O_2/H_2O}$ and $E_{F,H_2O_2/H_2O(Autocat.)}$ are employed to emphasize the Gaussian distribution of the energy states of H_2O_2 as the electron acceptor in the formal and autocatalytic electroreduction reactions, respectively.

cathodic current drift is further reinforced after the addition of 8 mM H_2O_2 to PBS, as manifested in another comparative study of the cyclic voltammograms (red solid and black dashed lines) collected exclusively for Ag NWs/CC (Fig. 3a). This was attributed to H_2O_2 electroreduction, most likely via the alternative autocatalytic mechanism (Eqs. 3 and 4),

$$H_2O_2 + H^+ + OH_{ad} + e^- \rightarrow 2OH_{ad} + H_2O, \quad (3)$$

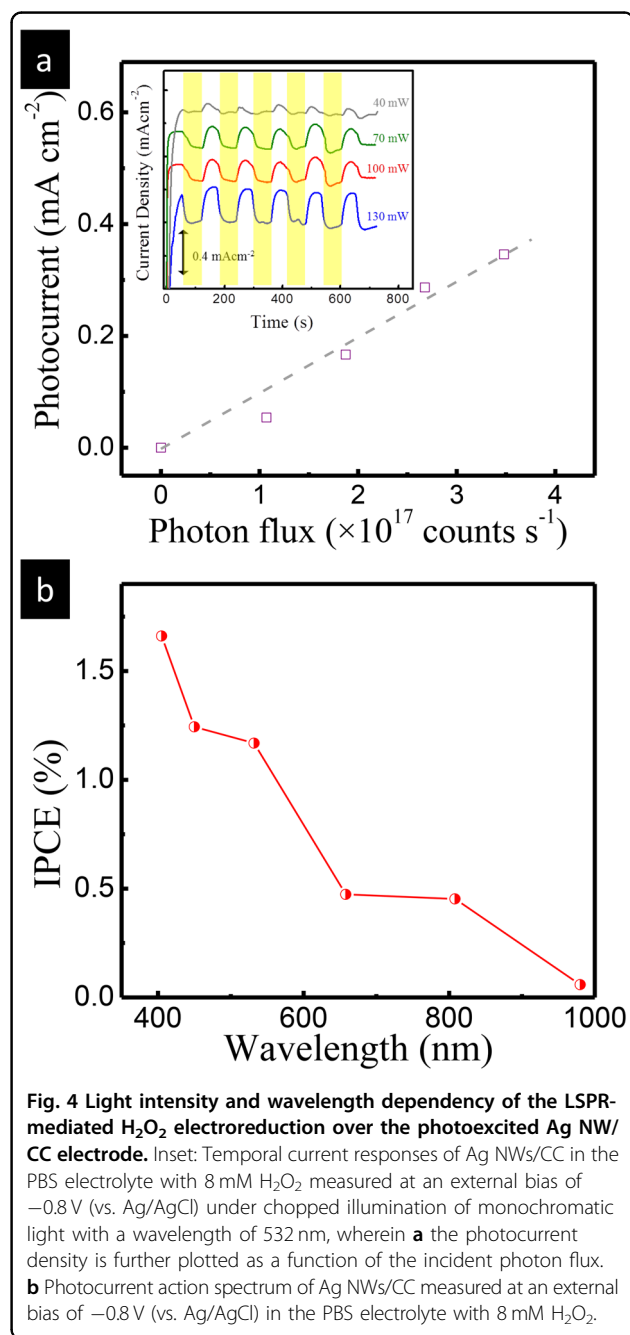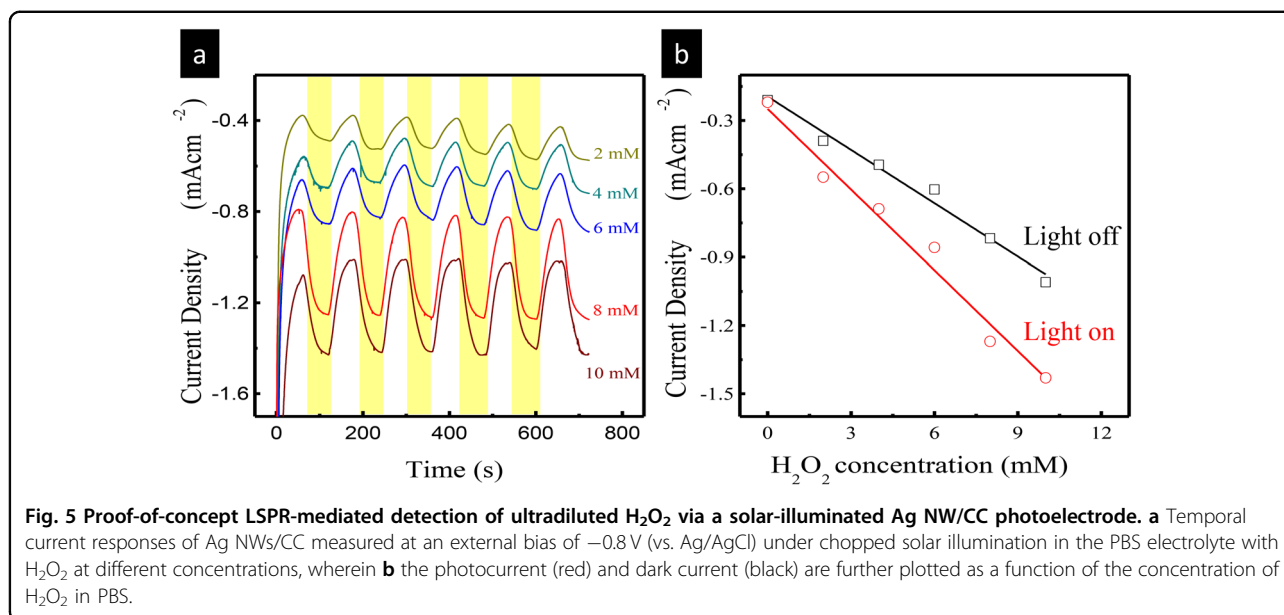$$OH_{ad} + H^+ + e^- \rightarrow H_2O. \quad (4)$$

for which the overpotential threshold has been reported to be much lower than that for the formal mechanism (Eqs. 1 and 2)[20,21]. From Eqs. 1–4, one can readily conclude that such overpotential alleviation benefits from the OH_{ad} adsorbate that, in the present study, is presumably derived from the chemisorption of the hydroxide ions (OH^-) in PBS onto the Ag NWs, as evidently reflected in

the redox pairs seen in the collected CV curve (black dashed line) of Ag NWs/CC[15]. The dependence of this faradaic cathodic current on autocatalytic H_2O_2 electroreduction is additionally illustrated schematically in the energy diagrams (first panel in Fig. 3e), wherein the formal H_2O_2 electroreduction is also highlighted. Upon further exposure of Ag NWs/CC to simulated sunlight, a similar cathodic current shift was again observed (Fig. 3b), stemming from the LSPR-mediated and/or LSPR-accelerated formal and/or autocatalytic H_2O_2 electroreduction along with Ag^+ electroreduction primarily via energetic electron injection from Ag NWs/CC to these species, as elaborated below. The broadband solar illumination first excites T- and L-LSPRs of Ag NWs/CC (second panel of Fig. 3e), which then relax via a nonradiative Landau damping process to generate hot electron–hole pairs (third panel of Fig. 3e)[4–11]. In view of the characteristic photoabsorption of the Ag NWs peaking at a wavelength of ~400 nm, corresponding to a photon energy of ~3.1 eV (Fig. 2c), most electrons transition to energy states well above the Fermi levels (E_F) of not only the Ag NWs but also the autocatalytic and formal H_2O_2/H_2O redox couples ($E_{F,H_2O_2/H_2O(Autocat.)}$ and $E_{F,H_2O_2/H_2O}$) by several eV. This appreciable energy mismatch renders the excited electrons hardly injected directly into H_2O_2 and Ag^+ for electroreduction. Alternatively, these hot carriers experience intensive electron–electron scattering, and their energy is spread across many additional electrons (fourth panel of Fig. 3e)[4–11]. With this energy input, numerous electrons are thermalized to an elevated temperature (designated as energetic electrons), leading to an increased population in the high-energy tail of the Fermi–Dirac distribution, and most importantly, these electrons are readily injected into H_2O_2 and Ag^+ to expedite and activate the autocatalytic and formal electroreduction[5–7]. This is well attested by the distinct cathodic photocurrent jumps highlighted in the chronoamperometric curve of Ag NWs/CC collected under chopped light illumination at a constant potential of −0.2 V (vs. Ag/AgCl) in Fig. 3c. On the other hand, the LSPR of plasmonic Ag could dephase through a radiative pathway to re-emit resonant photons (second and third panels of Fig. 3f), in which only UV photons have been reported to be effective in exciting H_2O_2 via the intramolecular highest occupied molecular orbital − lowest unoccupied molecular orbital (LUMO) electronic transitions (fourth panel of Fig. 3f)[4–6,23]. In this context, only a minority of the excited electrons successfully populate the LUMO of H_2O_2, which are then transferred to the Ag metal, as demonstrated by the relatively poor cathodic photocurrent drop in lieu of the jump seen in the chronoamperometric curve of the reference Ag thin film deposited on a fluorine-doped tin oxide (FTO)-coated glass substrate via thermal evaporation (Fig. 3d). Such discrepancy in the LSPR-mediated charge transfer kinetics is most likely attributed to the

nanostructure of the Ag NWs, favoring the relaxation of the characteristic LSPR preferentially via the nonradiative Landau damping process[4–11].

In this context, the more the LSPR of Ag NWs/CC is excited by the incident light, the more energetic electrons are generated and transferred to H_2O_2 for the formal and autocatalytic electroreduction. This is validated by the gradually enhanced photocurrent density measured for Ag NWs/CC subject to progressively intensified monochromatic illumination with a wavelength of 532 nm (inset in Fig. 4a). More importantly, the linear dependency

Fig. 4 Light intensity and wavelength dependency of the LSPR-mediated H_2O_2 electroreduction over the photoexcited Ag NW/CC electrode. Inset: Temporal current responses of Ag NWs/CC in the PBS electrolyte with 8 mM H_2O_2 measured at an external bias of −0.8 V (vs. Ag/AgCl) under chopped illumination of monochromatic light with a wavelength of 532 nm, wherein **a** the photocurrent density is further plotted as a function of the incident photon flux. **b** Photocurrent action spectrum of Ag NWs/CC measured at an external bias of −0.8 V (vs. Ag/AgCl) in the PBS electrolyte with 8 mM H_2O_2.

Fig. 5 Proof-of-concept LSPR-mediated detection of ultradiluted H_2O_2 via a solar-illuminated Ag NW/CC photoelectrode. a Temporal current responses of Ag NWs/CC measured at an external bias of −0.8 V (vs. Ag/AgCl) under chopped solar illumination in the PBS electrolyte with H_2O_2 at different concentrations, wherein **b** the photocurrent (red) and dark current (black) are further plotted as a function of the concentration of H_2O_2 in PBS.

of the photocurrent response of Ag NWs/CC on the irradiation intensity further reinforces this conclusion, as elucidated below (Fig. 4a)[4−8]. In addition to the charge transfer across the Ag NW/H_2O_2 solid–liquid boundary, the energetic electrons can alternatively experience electron–phonon scattering, by which their energy is dissipated into heating of the Ag NWs. As a result, the Ag NWs are thermalized to an elevated temperature, highly likely activating and/or accelerating the reaction rate of the formal and autocatalytic H_2O_2 electroreduction and resulting likewise in the photocurrent flow seen in the present study (inset in Fig. 4a)[9−11]. Such thermally driven chemical reactions have, however, been well acknowledged to follow the Arrhenius law, which suggests an exponential correlation between the photocurrent density and the light intensity, in contrast with the linear relationship derived in this work (Fig. 4a)[4−11]. In this regard, one can conclude that in the present model system, the contribution of the LSPR-induced thermalization of Ag NWs/CC to the photocurrent reinforcement plays only a minor role (see Supplementary Note 1 for details). Last but not least, the efficiency of the LSPR-mediated energetic electron injection from Ag NWs/CC to H_2O_2 was further evaluated in terms of the IPCE, for which the wavelength dependency was highlighted via the photocurrent action spectrum (Fig. 4b). Excellent agreement with the characteristic optical absorption spectrum of the Ag NWs plotted alongside for comparison is perceived (Supplementary Fig. S3). This, along with the foregoing analyses discussed above, offers three pieces of evidence for the H_2O_2 photoelectrochemical reduction in the present study at the phase boundary with Ag NWs/CC

proceeding via the LSPR-mediated charge transfer mechanism[4−8].

On the other hand, the photocurrent density of Ag NWs/CC depends further on the concentration of H_2O_2 in PBS, as highlighted by the chronoamperometric curves collected at a constant potential of −0.8 V (vs. Ag/AgCl) under chopped solar irradiation (Fig. 5a). This supports that H_2O_2 photoelectrochemical reduction contributes a cathodic faradaic current to the measured photoresponse of Ag NWs/CC, which, surprisingly, is well resolved even if the concentration of H_2O_2 in PBS is dropped to 2 mM. This in turn emphasizes the good prospect of plasmonic Ag NWs/CC in the analytical biochemistry field, provided that such ultralow detection limits along with decent longevity are of great interest to such applications (Fig. 5a and Supplementary Fig. S4)[13,14,16]. Moreover, the sensitivity of Ag NWs/CC for the photoelectrochemical detection of H_2O_2 in PBS at a trace level of less than 10 mM, derived from the concentration-dependent photocurrent responses, amounts to $118\,\mu A\,cm^{-2}\,mM^{-1}$ (Fig. 5b). This not only far exceeds that ($78\,\mu A\,cm^{-2}\,mM^{-1}$) inferred from the dark current flows for Ag NWs/CC collected in the absence of solar illumination but also is among the highest performance reported for enzyme-free Ag-based electrochemical H_2O_2 detectors in the literature (Fig. 5b and Supplementary Table S1).

Conclusions

Overall, the LSPR-mediated charge transfer kinetics of Ag NWs/CC at the liquid junction with H_2O_2 in PBS for solar photoelectrochemical reduction were systematically explored in the present study. XRD, SEM, and TEM

results demonstrated that the plasmonic Ag metal was engineered in a wire-like nanostructure. In this way, the resonant wavelengths of the characteristic T- and L-LSPRs of the Ag NWs were well extended over the broadband solar spectrum, as manifested in the collected UV–Vis spectrum. This in turn allowed the Ag NWs to take full advantage of the solar energy for LSPR-mediated energetic electron generation and transfer through the liquid junction to H_2O_2 in PBS for electroreduction, as attested by the wavelength dependency of the IPCE highlighted by the photocurrent action spectrum and the linear light intensity dependency of the photoresponse of Ag NWs, respectively. In these measurements, the Ag NWs were deposited directly on a CC substrate to formulate the Ag NW/CC working electrode, for which the photocurrent was tracked by means of CV and chronoamperometry. In addition to the mechanistic insights, the work presented herein further highlighted the great promise of such LSPR-mediated charge kinetics of Ag NWs/CC in the analytical biochemistry field via proof-of-concept solar photoelectrochemical detection of ultra-diluted H_2O_2 in PBS. The sensitivity of the solar-illuminated Ag NW/CC photoelectrode amounted to 118 $\mu A\,cm^{-2}\,mM^{-1}$, far exceeding that of the electrochemical counterpart measured in the dark by 50%.

Conflict of interest
The authors declare that they have no conflict of interest.

Publisher's note
Springer Nature remains neutral with regard to jurisdictional claims in published maps and institutional affiliations.

Supplementary information is available for this paper at https://doi.org/10.1038/s41427-020-00259-8.

References
1. Linic, S., Christopher, P. & Ingram, D. B. Plasmonic-metal nanostructures for efficient conversion of solar to chemical energy. *Nat. Mater.* **10**, 911–921 (2011).
2. Zhang, X., Chen, Y. L., Liu, R. S. & Tsai, D. P. Plasmonic photocatalysis. *Rep. Prog. Phys.* **76**, 046401 (2013).
3. Thrall, E. S., Steinberg, A. P., Wu, X. & Brus, L. E. The role of photon energy and semiconductor substrate in the plasmon-mediated photooxidation of citrate by silver nanoparticles. *J. Phys. Chem. C* **117**, 26238–26247 (2013).
4. Meng, X. et al. Nanometals for solar-to-chemical energy conversion: from semiconductor-based photocatalysis to plasmon-mediated photocatalysis and photo-thermocatalysis. *Adv. Mater.* **28**, 6781–6803 (2016).
5. Linic, S., Aslam, U., Boerigter, C. & Morabito, M. Photochemical transformations on plasmonic metal nanoparticles. *Nat. Mater.* **14**, 567–576 (2015).
6. Kale, M. J., Avanesian, T. & Christopher, P. Direct photocatalysis by plasmonic nanostructures. *ACS Catal.* **4**, 116–128 (2014).
7. Boerigter, C., Campanal, R., Morabito, M. & Linic, S. Evidence and implications of direct charge excitation as the dominant mechanism in plasmon-mediated photocatalysis. *Nat. Commun.* **7**, 10545 (2016).
8. Schlather, A. E. et al. Hot hole photoelectrochemistry on Au@SiO_2@Au nanoparticles. *J. Phys. Chem. Lett.* **8**, 2060–2067 (2017).
9. Swearer, D. F. et al. Plasmonic photocatalysis of nitrous oxide into N_2 and O_2 using aluminum—iridium antenna—reactor nanoparticles. *ACS Nano* **13**, 8076–8086 (2019).
10. Zhou, L. et al. Quantifying hot carrier and thermal contributions in plasmonic photocatalysis. *Science* **362**, 69–72 (2018).
11. Zhang, X. et al. Plasmon-enhanced catalysis: distinguishing thermal and nonthermal effects. *Nano Lett.* **18**, 1714–1723 (2018).
12. Sanz, J. M. et al. UV plasmonic behavior of various metal nanoparticles in the near- and far-field regimes: geometry and substrate effects. *J. Phys. Chem. C* **117**, 19606–19615 (2013).
13. Chen, Y. C., Hsu, J. H. & Hsu, Y. K. Branched silver nanowires on an FTO support for simultaneous amperometric detection of H_2O_2 and of 4-aminothiophenol by SERS. *Microchim. Acta* **185**, 106 (2018).
14. Chen, Y. C., Hsu, J. H., Lin, Y. G. & Hsu, Y. K. Silver nanowires on coffee filter as dual-sensing functionality for efficient and low-cost SERS substrate and electrochemical detection. *Sens. Actuators B Chem.* **245**, 189–195 (2017).
15. Marenco, A. J., Pedersen, D. B., Wang, S., Petryk, M. W. P. & Kraatz, H. B. Electrochemical properties of gas-generated silver nanoparticles in the presence of cyano- and chloride-containing compounds. *Analyst* **134**, 2021–2027 (2009).
16. Kurowska, E., Brzózka, A., Jarosz, M., Sulka, G. D. & Jaskuła, M. Silver nanowire array sensor for sensitive and rapid detection of H_2O_2. *Electrochim. Acta* **104**, 439–447 (2013).
17. Plauck, A., Stangland, E. E., Dumesic, J. A. & Mavrikakis, M. Active sites and mechanisms for H_2O_2 decomposition over Pd catalysts. *Proc. Natl Acad. Sci. USA* **113**, E1973–E1982 (2016).
18. Li, X., Heryadi, D. & Gewirth, A. A. Electroreduction activity of hydrogen peroxide on Pt and Au electrodes. *Langmuir* **21**, 9251–9259 (2005).
19. Choi, C. H. et al. Unraveling the nature of sites active toward hydrogen peroxide reduction in Fe-N-C catalysts. *Angew. Chem. Int. Ed.* **56**, 8809–8812 (2017).
20. Flätgen, G. et al. Autocatalytic mechanism of H_2O_2 reduction on Ag electrodes in acidic electrolyte: experiments and simulations. *Electrochim. Acta* **44**, 4499–4506 (1999).
21. Shafei, M. & Honeychurch, K. C. Voltammetric behaviour of hydrogen peroxide at a silver electrode fabricated from a rewritable digital versatile disc (DVD) and its determination in water samples. *Anal. Methods* **5**, 6631–6636 (2013).
22. Gebeyehu, M. B., Chala, T. F., Chang, S. Y., Wu, C. M. & Lee, J. Y. Synthesis and highly effective purification of silver nanowires to enhance transmittance at low sheet resistance with simple polyol and scalable selective precipitation method. *RSC Adv.* **7**, 16139–16148 (2017).
23. Goldstein, S., Aschengrau, D., Diamant, Y. & Rabani, J. Photolysis of aqueous H_2O_2: quantum yield and applications for polychromatic UV actinometry in photoreactors. *Environ. Sci. Technol.* **41**, 7486–7490 (2007).